Supplemental Material
Linear-time cluster ensembles of large-scale single-cell RNA-seq and multimodal data

Van Hoan Do[1], Francisca Rojas Ringeling[1], and Stefan Canzar*[1]

[1]Gene Center, Ludwig-Maximilians-Universität München, Munich, Germany

1 Supplemental Notes

Supplemental Note 1. Specter tailors landmark-based clustering to the analysis of single cells

We show results for three variants of Specter in which we either replace the k-means based landmark selection or the selective sampling approach by standard random sampling, or in which we omit the clustering ensemble step altogether. Supplemental Figures S5 and S6 demonstrate the effectiveness of our adoptions and extensions of the original algorithm to the analysis of scRNA-seq data. Across all 24 simulated data sets, Specter achieved a higher ARI (mean ARI 0.89) than LSC (mean ARI 0.59) (Supplemental Figure S5). In fact, even without the benefit of a clustering ensemble, further algorithmic adjustments implemented in Specter such as a modified bandwidth of the Gaussian kernel yielded an improvement over LSC on 19 out of 24 data sets. When disabling the clustering ensemble approach in Specter, however, its performance decreased consistently, on several data sets the decrease in ARI was substantial. Similarly, on 21 out of 24 data sets the selective sampling in Specter was more effective in terms of ARI than random sampling. On two instances with unbalanced cell type compositions (*pbmc*), the score more than doubled. Coupled with random sampling (instead of selective sampling), the consensus clustering obtained from a clustering ensemble was often even less accurate than a single clustering. The hybrid k-means based landmark selection led to an improvement in ARI on all but one data sets (Supplemental Figure S6). In many cases this improvement was substantial, especially on difficult instances with unbalanced cell type compositions (*pbmc*, G*neq*).

Supplemental Note 2. Specter benefits from a small number of ensemble members and is robust to choice of parameter γ

In Supplemental Figure S7 we further addressed the dependence of Specter's accuracy on the number of ensemble members from which Specter computes a consensus clustering. Consistent with our observation in Supplemental Figure S5, the clustering ensemble approach yielded on average more accurate results on the 24 simulated data sets than relying on a single clustering for each data set. Even a small number of ensemble members (e.g. 10) improved clustering accuracy substantially, while only minor improvements were achieved when increasing their number further to more than

*Correspondence: canzar@genzentrum.lmu.de

20 ensemble members. Nevertheless, a clustering ensemble of size 200 yielded highest mean ARI with lowest score variance.

Finally, we demonstrate robustness of Specter to the choice of parameter γ that controls the bandwidth of the Gaussian kernel that is set differently in Specter compared to LSC (Methods). Even though this parameter is randomly selected from interval $[0.1, 0.2]$ consistently across all 45 data sets in this benchmark, Supplemental Figure S8 shows that with very few exceptions choosing γ from different intervals would yield nearly identical results.

2 Supplemental Tables

Supplemental Table S1: Overview of the real data sets used in this study. Names listed in the left-most column are used throughout the text. A line separates data sets in which cell type labels were inferred from scRNA-seq measurements from data set were labels are based on cell phenotypes defined independently of scRNA-seq.

Data set	# Cells	# Populations	Description	Reference
grun	1502	2	mouse stem cells	Grün et al. 2016
xin	1600	8	human islet cells	Xin et al. 2016
baron	1886	13	human and mouse pancreas	Baron et al. 2016
biase	56	4	mouse embryo devel	Biase et al. 2014
deng-1	268	6	mouse embryo devel (RPKMs)	Deng et al. 2014
deng-2	268	6	mouse embryo devel (Reads)	Deng et al. 2014
goolam	114	5	mouse embryo	Goolam et al. 2016
muraro	2126	10	human pancreas	Muraro et al. 2016
patel	430	5	human glioblastoma	Patel et al. 2014
pollen	301	11	human developing cortex	Pollen et al. 2014
klein	2717	4	mouse embryo stem cells	Klein et al. 2015
zeisel	3005	9	mouse cortex and hippocampus	Zeisel et al. 2015
chen	14,437	45	mouse brain	Chen et al. 2017
CNS	465,281	7	mouse central nervous system	Zeisel et al. 2018
saunders	665,858	11	adult mouse brain	Saunders et al. 2018
trapnell	2,058,652	38	mouse organogenesis cell atlas	Cao et al. 2019
Koh	531	9	human embryonic stem cells	Koh et al. 2016
Kumar	246	3	mouse embryonic stem cells	Kumar et al. 2014
Zhengmix4eq	3,994	4	mixture of purified PBMCs	Zheng et al. 2017
Zhengmix4uneq	6,498	4	mixture of purified PBMCs	Zheng et al. 2017
Zhengmix8eq	3,994	8	mixture of purified PBMCs	Zheng et al. 2017

Supplemental Table S2: Overview of the simulated data sets used in this study. Names listed in the left-most column are used throughout the text. Data sets were simulated using Splatter (Zappia et al. 2017) and vary in number of cells (#Cells), number of genes (#Genes), number of clusters (k), the probability with which a given gene is differentially expressed in one of the cell types (marker genes), and the relative abundance of cell types that were either equal, unequal, or based on cell type abundances among peripheral blood mononuclear cells (PBMCs) in healthy individuals.

Name	# Cells	# Genes	k	Probabilities	Relative
	(N)	(D)		of gene DE	abundances (G)
DE1GeqN1k	1,000	1,000	5	(0.01, 0.01 0.01, 0.01, 0.01)	(0.2, 0.2, 0.2, 0.2, 0.2)
DE1GeqN2k	2,000	1,000	5		
DE1GeqN5k	5,000	1,000	5		
DEneqGneqN1k	1,000	1,000	5	(0.01, 0.01 0.02, 0.02, 0.05)	(0.01, 0.05, 0.14, 0.3, 0.5)
DEneqGneqN2k	2,000	1,000	5		
DEneqGneqN5k	5,000	1,000	5		
DEneqGneqN1kD10k	1,000	10,000	5	(0.01, 0.01 0.02, 0.02, 0.05)	(0.01, 0.05, 0.14, 0.3, 0.5)
DEneqGneqN2kD10k	2,000	10,000	5		
DEneqGneqN5kD10k	5,000	10,000	5		
DE1GneqN1k	1,000	1,000	5	(0.01, 0.01 0.01, 0.01, 0.01)	(0.01, 0.05, 0.14, 0.3, 0.5)
DE1GneqN2k	2,000	1,000	5		
DE1GneqN5k	5,000	1,000	5		
DE1GneqN1kD10k	1,000	10,000	5	(0.01, 0.01 0.01, 0.01, 0.01)	(0.01, 0.05, 0.14, 0.3, 0.5)
DE1GneqN2kD10k	2,000	10,000	5		
DE1GneqN5kD10k	5,000	10,000	5		
DE2GneqN1k	1,000	1,000	5	(0.02, 0.02 0.02, 0.02, 0.02)	(0.01, 0.05, 0.14, 0.3, 0.5)
DE2GneqN2k	2,000	1,000	5		
DE2GneqN5k	5,000	1,000	5		
DE5GneqN1k	1,000	1,000	5	(0.05, 0.05 0.05, 0.05, 0.05)	(0.01, 0.05, 0.14, 0.3, 0.5)
DE5GneqN2k	2,000	1,000	5		
DE5GneqN5k	5,000	1,000	5		
DE1GpbmcN1k	1,000	1,000	5	(0.01, 0.01 0.01, 0.01, 0.01)	PBMCs: DC: 0.02, NK: 0.2, B: 0.1 Mono: 0.08, T: 0.6
DE1GpbmcN2k	2,000	1,000	5		
DE1GpbmcN5k	5,000	1,000	5		
RareCellExp1	4,000	1,000	2	(0.01, 0.01)	(0.5, 0.5)
RareCellExp2	10,000	1,000	2	(0.01, 0.01)	(0.9, 0.1)

Supplemental Table S3: Markers used in the annotation of clusters in the CBMC and PBMC data sets. P-values indicate significance of differential expression according to a Wilcoxon rank-sum test between clusters inferred by Specter from the joint analysis of mRNA and surface protein expression.

Cell-type	Data set	Markers
$CD8^+CD27^-$	PBMC	*CD8A* (p = 3.1e-15), *CD8B* (p = 4.3e-6), low *CD27* ADT
$CD8^+CD27^+$	PBMC	*CD8B* (p = 3.2e-4), high *CD27* ADT
Naive $CD4^+$ T	PBMC	*SELL* (Haining et al. 2008) (p = 2.6e-9)
$CD4^+CD27^+$	PBMC	*IL7R* (Colpitts et al. 2009) (p = 9.4e-11), high *CD27* ADT
$CD4^+CD27^-DR^+$	PBMC	*IL7R* (Colpitts et al. 2009) (p = 4.4e-7), *NKG7* (Fonseka et al. 2018)(p = 1.2e-3), *GZMA* (Fonseka et al. 2018) (p = 2.0e-4)
$CD4^+CD27^-DR^-$	PBMC	*IL7R* (Colpitts et al. 2009) (p = 1.4e-6), low expression of *NKG7* and *GZMA*; low *CD27* ADT.
$CD14^+$ Mono	PBMC	*LYZ* (p = 7.5e-34), *CST3* (p = 1.4e-32)
$FCGR3A^+$ Mono	PBMC	*FCGR3A* (p = 1.0e-9)
Megakaryocytes	PBMC	*PF4* (Lambert, Meng, Xiao, et al. 2016) (p = 1.2e-3)
NK	PBMC	*GNLY* (Ogawa et al. 2003) (p = 7.7e-21), *NKG7* (Turman et al. 1993)(p = 1.1e-15)
Dendritic cells	CBMC	*CST3* (Hruz et al. 2008) (p = 4.7e-29), *CD1C* (Collin et al. 2013; Merad et al. 2013) (p = 1.1e-27), and *FCER1A* (Hruz et al. 2008) (p = 1.3e-27)
Megakaryocytes	CBMC	*PF4* (Lambert, Meng, Harper, et al. 2014) (p = 1.6e-25), *PPBP* (Sakurai et al. 2016) (p = 5.8e-24)

Supplemental Table S4: Comparison of running times in minutes on simulated data. Data sets of different size were simulated using Splatter. *Running times exclude preprocessing for all methods except TSCAN and dropClust, whose implementation did not allow to isolate the core algorithm. Specter used 20 ensemble members and was run with a single thread (as all other methods). The last column (Specter+Pre) shows the total running time of Specter and all its preprocessing steps, including log-transformation, selection of highly variable genes (500), and PCA.

#Cells	Specter	Seurat	dropClust*	Geosketch	RtsneKmeans	TSCAN*	Specter+Pre
1k	0.02	0.04	0.04	0.10	0.14	0.06	0.02
10k	0.1	0.15	0.24	0.02	0.88	0.20	0.1
100k	0.58	1.00	1.01	1.38	17.61	1.23	0.61
200k	1.36	3.27	1.89	1.75	49.31	2.79	1.40
500k	3.15	11.80	3.14	8.81	139.69	7.39	3.25
1m	7.59	23.00	6.83	44.29	655.95	16.61	7.77

Supplemental Table S5: Running times of the MATLAB PCA implementation (Vijayan 2020) used in Specter and FIt-tSNE (Linderman et al. 2019) on simulated data. Data sets of different size were simulated using Splatter (same data sets as in Table S4).

Method	1k	10k	100k	200k	500k	1m
PCA	0.04s	0.12s	0.52s	1.59s	3.43s	5.98s
FIt-SNE	41s	1m17s	1m4s	1m53s	4m3s	8m11s

Supplemental Table S6: Comparison of running times on three largest real data sets. Running times of Specter, Seurat, dropClust, the geometric sketching (Gsketch) based Louvain clustering, TSCAN, and RtsenKmeans are reported in minutes (rounded) on the 3 largest real data sets used in this study. *Running times exclude preprocessing for all methods except TSCAN and dropClust, whose implementation did not allow to isolate the core algorithm. Specter used 50 ensemble members and was run with 20 threads. The last column (Specter+Pre) shows the total running time of Specter and all its preprocessing steps, including log-transformation, selection of highly variable genes (2000), and PCA.

Data set	#Cells	Specter	Seurat	dropClust*	Gsketch	TSCAN*	RtsneKmeans	Specter+Pre
CNS	464,713	1	11	2	7	3	89	3
saunders	665,385	2	18	3	19	8	193	4
trapnell	2,026,641	15	79	12	400	100	1225	23

3 Supplemental Figures

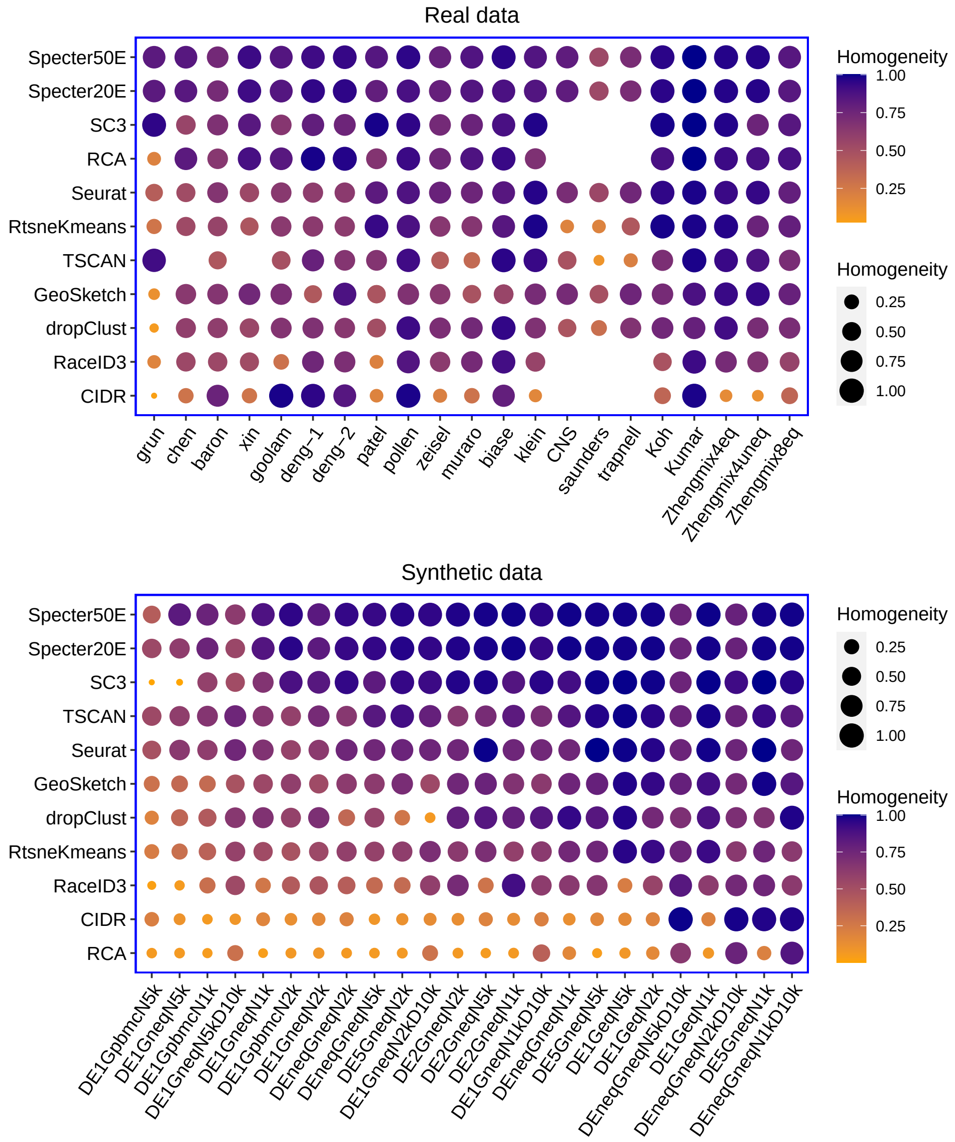

Supplemental Figure S1: Clustering performance measured by homogeneity score of Specter and competing methods on real and synthetic data. Methods are ordered by mean homogeneity score across data sets decreasing from top to bottom. In the calculation of mean scores we excluded for each method the data sets where the method did not run successfully. Synthetic data sets are ordered from left to right by increasing mean homogeneity score over all methods. SC3 , RCA, RaceID3, and CIDR failed to run on the three largest data sets *CNS*, *saunders*, and *trapnell* due to insufficient memory. TSCAN failed to run on data sets *chen* and *skin* for unknown reasons. Geometric sketching refers to the Louvain clustering of 10% of the cells sampled using geometric sketching.

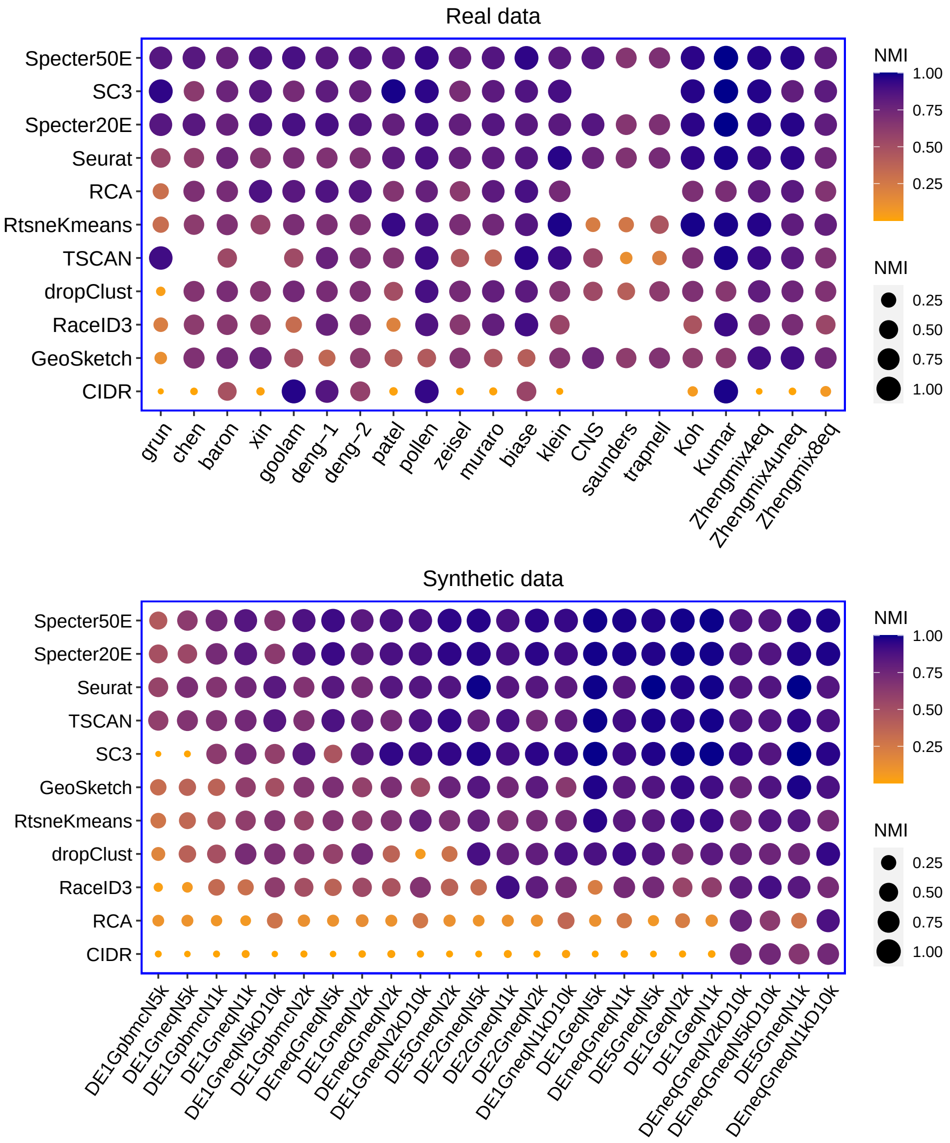

Supplemental Figure S2: Clustering performance measured by NMI of Specter and competing methods on real and synthetic data. Methods are ordered by mean NMI across data sets decreasing from top to bottom. In the calculation of mean scores we excluded for each method the data sets where the method did not run successfully. Restricted to the same set of data sets as SC3, Specter20E was with a mean ARI of 0.87 marginally better than SC3 (mean ARI 0.85). Synthetic data sets are ordered from left to right by increasing mean NMI over all methods. SC3 , RCA, RaceID3, and CIDR failed to run on the three largest data sets *CNS*, *saunders*, and *trapnell* due to insufficient memory. TSCAN failed to run on data sets *chen* and *skin* for unknown reasons. Geometric sketching refers to the Louvain clustering of 10% of the cells sampled using geometric sketching.

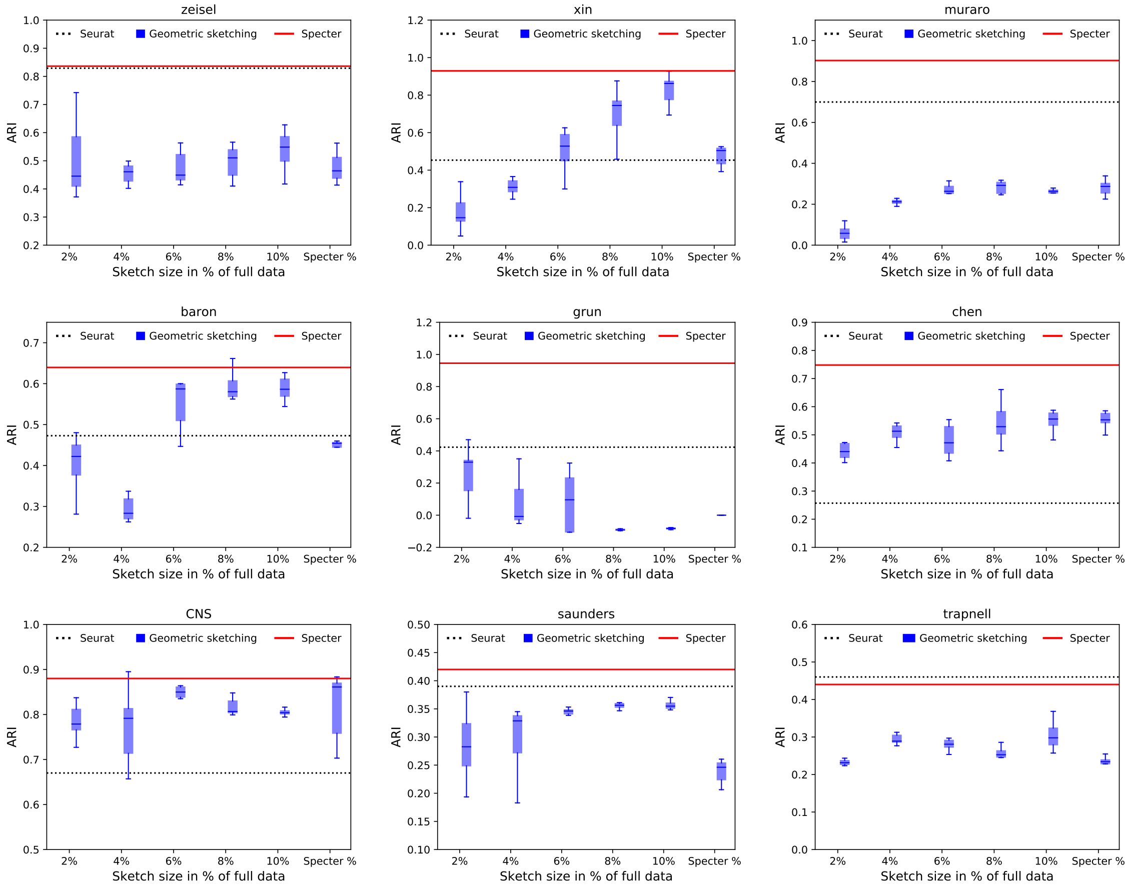

Supplemental Figure S3: Accuracy (in ARI) of geometric sketching based Louvain clustering for varying sketch sizes. For each sketch size, the results of 10 random trials are shown. "Specter %" uses the same number of cells in the geometric sketch as Specter uses landmarks or cells in the selective sampling step (see the "Methods" section), whichever one is larger.

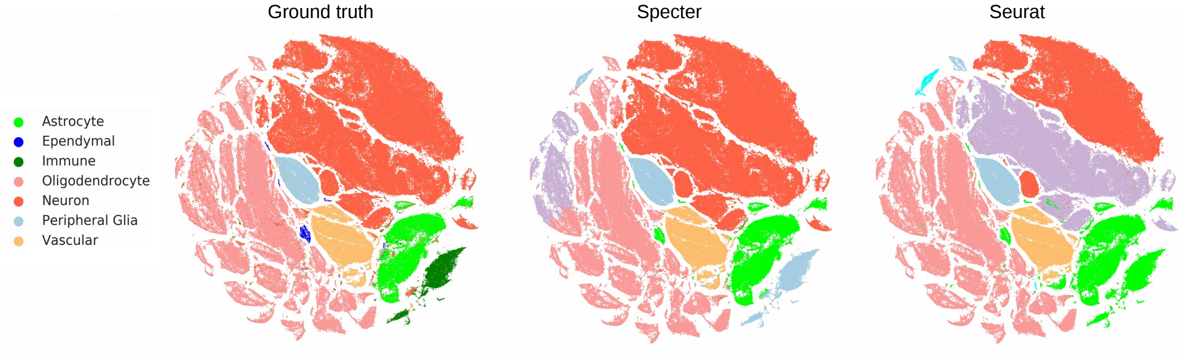

Supplemental Figure S4: t-SNE visualization of single cells of the mouse nervous system (data set *CNS*). Cells in the ground truth representation (left) are colored by cell type specified by the legend. The visualization of Specter (middle) and Seurat (right) clusterings use the same 2D embedding as the ground truth, but cells are colored according to clusters inferred by the two methods; colors do not directly reflect cell types specified by the legend. As expected by the higher ARI (0.89 vs 0.67) (and higher homogeneity scores of 0.81 vs 0.71 and NMI of 0.84 vs 0.78), Specter makes fewer mistakes. In contrast to Specter, Seurat wrongly splits neurons into 2 populations, is not able to distinguish astrocytes from immune cells, and is similarly not able to distinguish a subpopulation of vascular cells from astrocytes.

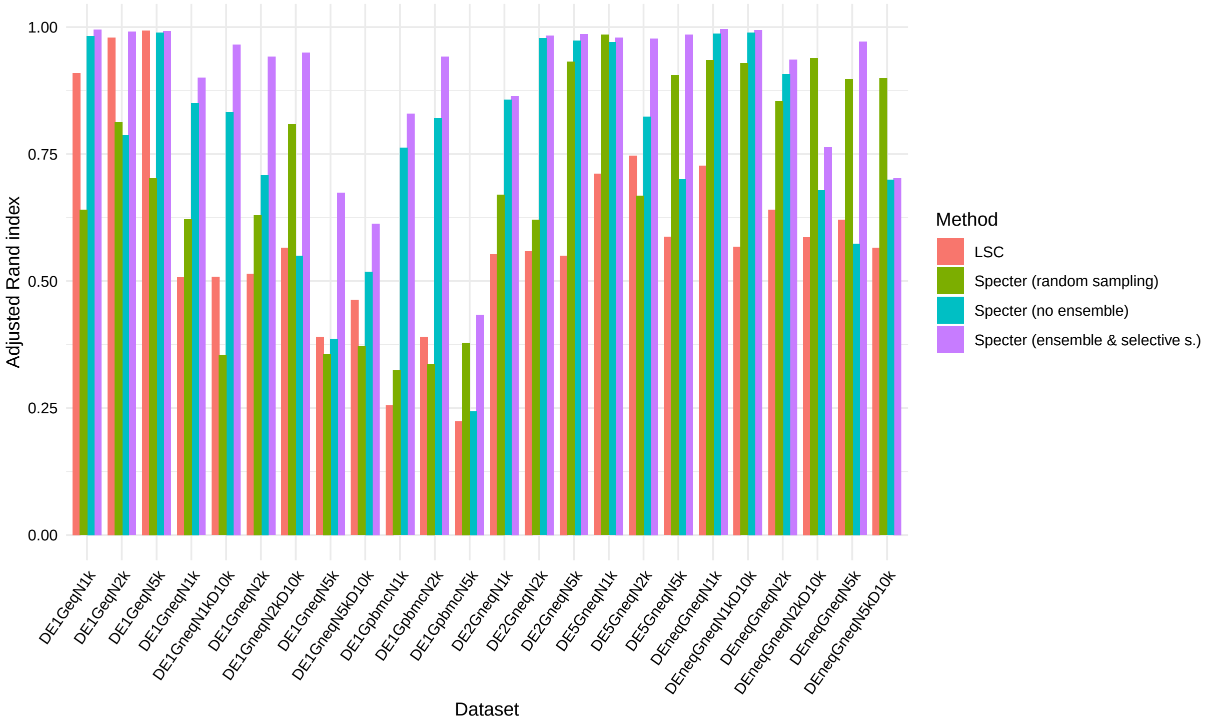

Supplemental Figure S5: Improvements in Specter over LSC. The clustering accuracy of Specter using 50 ensemble members (ensemble & selective s.) is compared to the accuracy of the original implementation of the landmark-based spectral clustering algorithm (LSC) and two variants of Specter in which we either disable consensus clustering in Specter (no ensemble) or in which we replace the novel selective sampling in Specter (Algorithm 2) by random sampling. When no clustering ensemble is used (no ensemble), we set parameters to the median values of intervals probed by the ensemble scheme ($\gamma = 0.15, p = 9k\log(k)$).

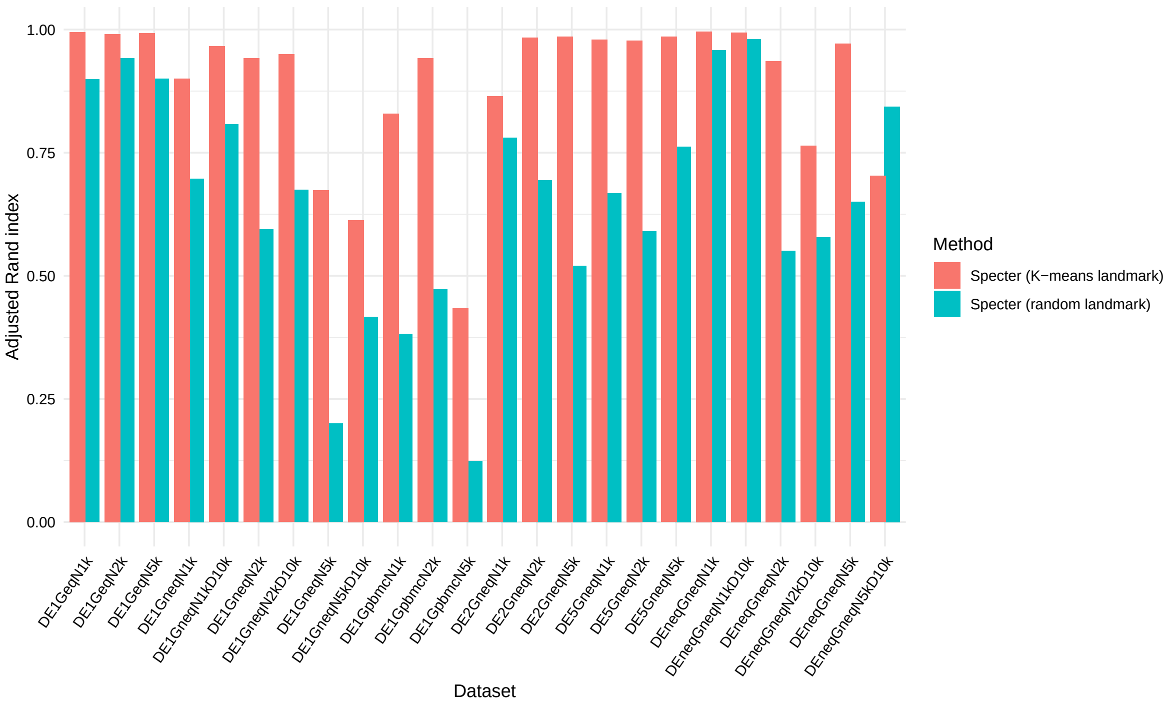

Supplemental Figure S6: Comarison of landmark selection strategies. The clustering accuracy of Specter using our hybrid k-means based landmark selection strategy (K-means landmark) is compared to a variant of Specter in which we select landmarks uniformly at random.

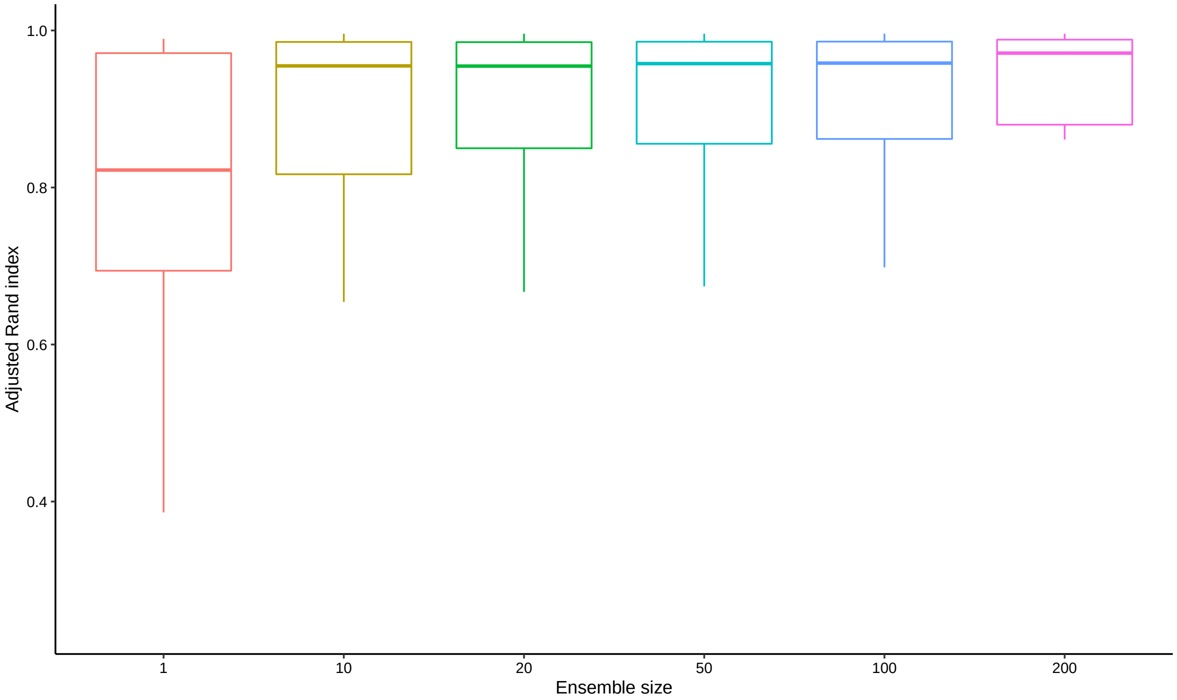

Supplemental Figure S7: Accuracy of Specter vs. number of ensemble members. For each number of ensemble members, the box plot shows minimum, maximum, median, and first and third quartiles of ARI scores achieved by Specter on the 24 simulated data sets described in Table S2.

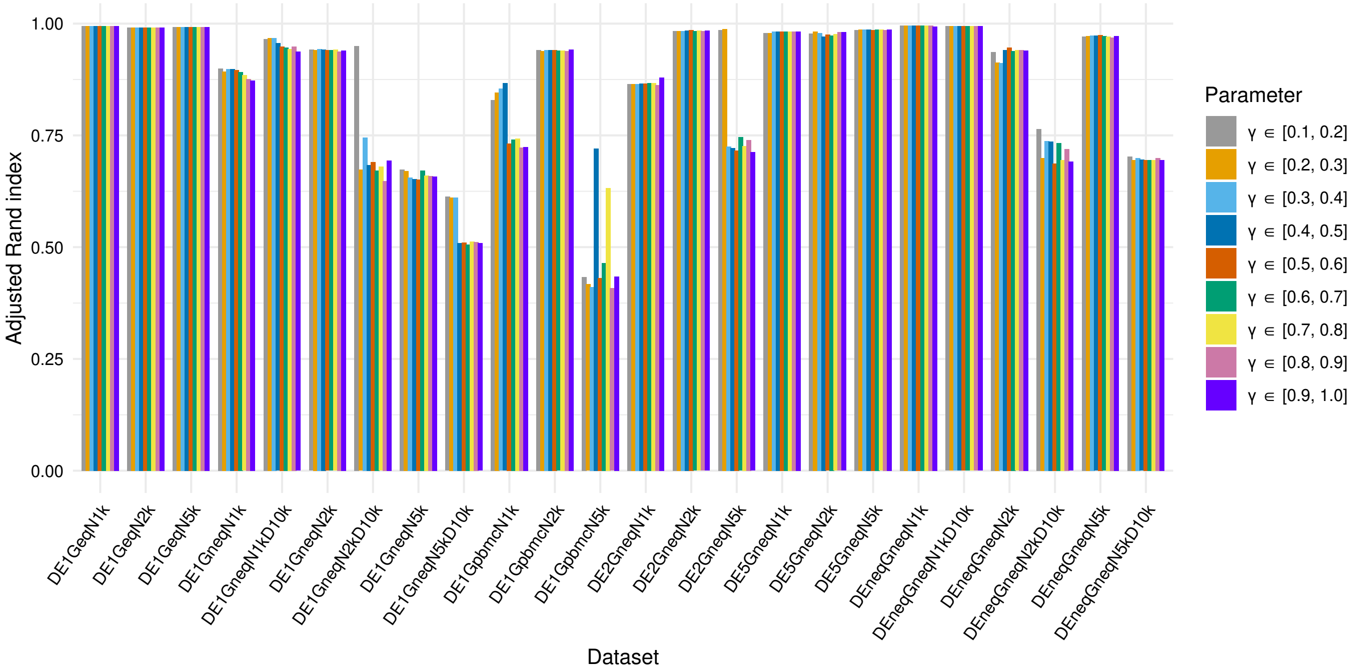

Supplemental Figure S8: Robustness of Specter to choice of parameter γ. Across 24 synthetic data sets, Specter computed 50 ensemble members using different ranges for parameter γ. By default, Specter selects a $\gamma \in [0.1, 0.2]$ for each ensemble member.

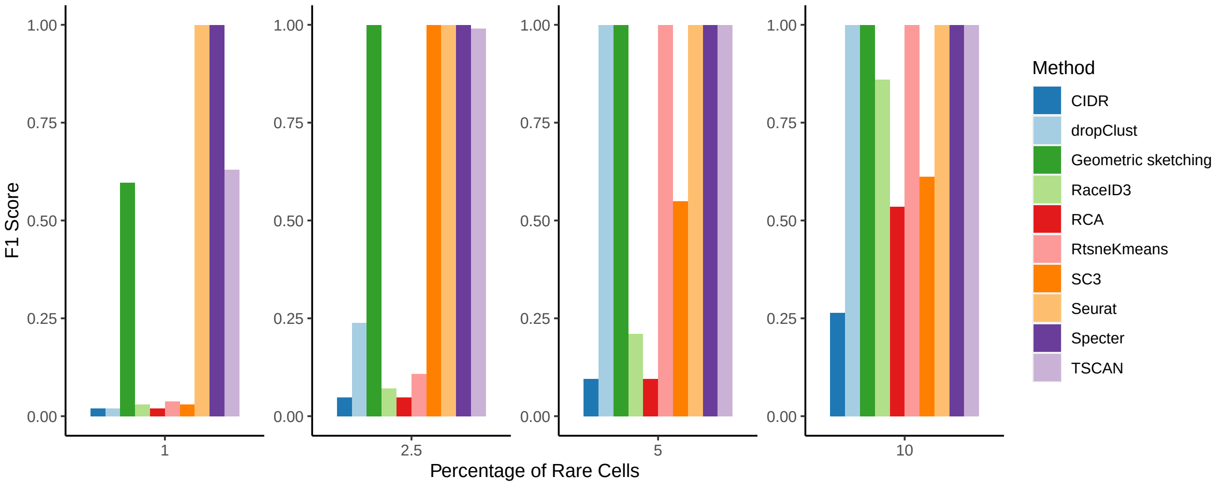

Supplemental Figure S9: Sensitivity to rare cell types with equal starting abundances. 4000 cells from two equal size groups (2000 cells each) were simulated using Splatter. We randomly downsampled one group to comprise 1%, 2.5%, 5%, and 10% of the total number of cells. We repeated this experiment five times for each group and show the average F_1 score over the 10 runs. For geometric sketching, the average F_1 score was taken over 10 random trials with a sketch size of 10% of the full data.

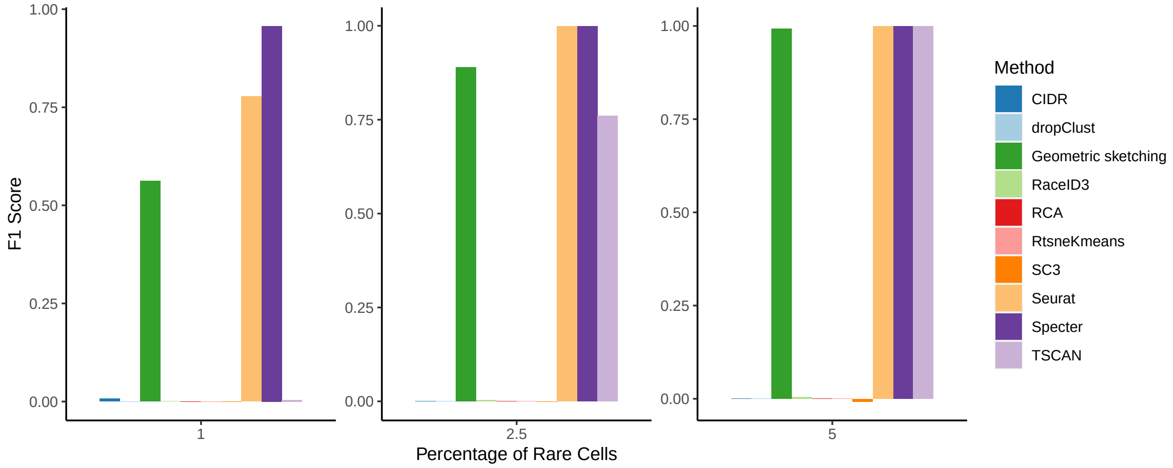

Supplemental Figure S10: Sensitivity to rare cell types in initially smaller group. Cells were randomly sampled from the smaller of two simulated groups (1,000 and 9,000 cells) to comprise 1%, 2.5%, and 5% of the total number of cells. We show the average F_1 score over 10 runs of this experiment. For geometric sketching, the average F_1 score was taken over 10 random trials with a sketch size of 10% of the full data.

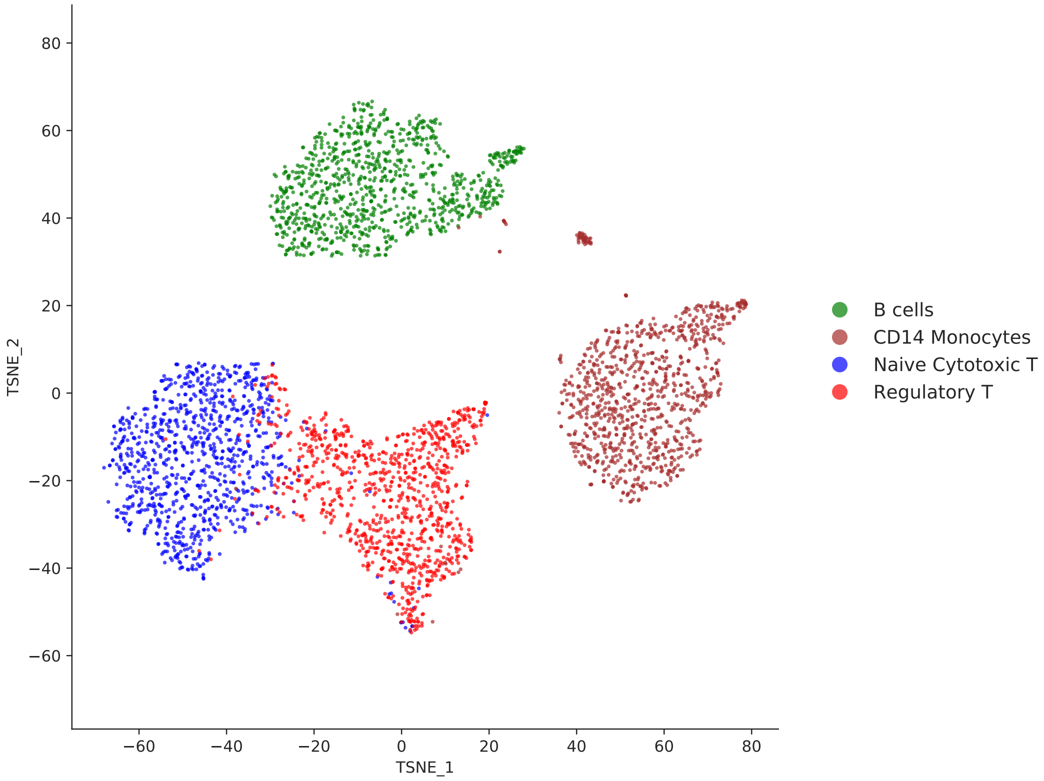

Supplemental Figure S11: t-SNE visualization of the Zhengmix4eq dataset (see Table S1). Naive cytotoxic T cells and regulatory T cells partly overlap.

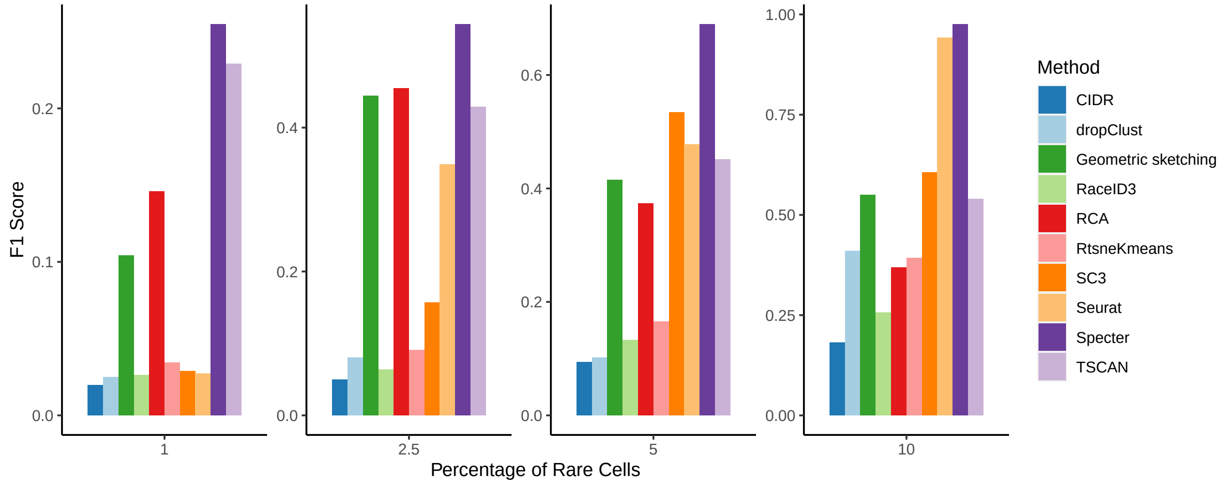

Supplemental Figure S12: Sensitivity to rare population of overlapping cell types. Naive cytotoxic T cells and regulatory T cells taken from the Zhengmix4eq data set overlap in the t-SNE projection shown in Figure S11. We randomly downsampled naive cytotoxic and regulatory T cells to comprise 1%, 2.5%, 5%, and 10% of the total number of cells and repeated this experiment five times for each group. Average F_1 scores are shown over the 10 runs, with adjusted F_1 score ranges for each subsample size. For geometric sketching, the average F_1 score was taken over 10 random trials with a sketch size of 10% of the full data.

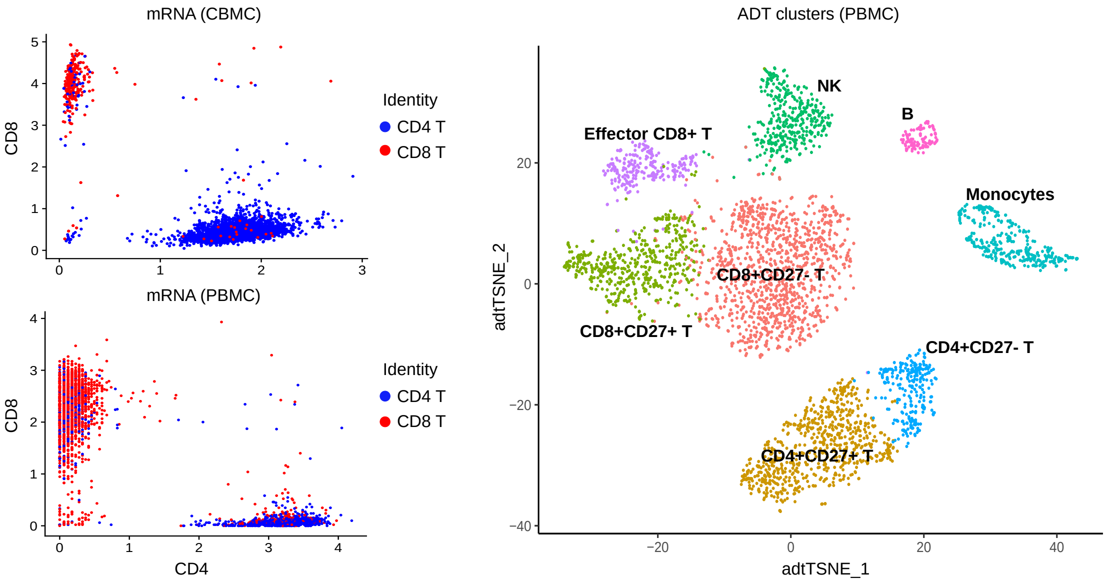

Supplemental Figure S13: Seurat unimodal clustering. *left:* CBMCs (top) and PBMCs (bottom) with coordinates of protein expression (ADT) along CD4 and CD8 axis. Colors denote clusters computed by Seurat based on mRNA expression which contain a mix of CD4 T cells and CD8 T cells. *right:* t-SNE visualization of clusters identified by Seurat from protein expression (ADT) of PBM cells. CD14$^+$ and FCGR3A$^+$ monocytes cannot be discriminated (compare Figure 6), megakaryocytes are not detected.

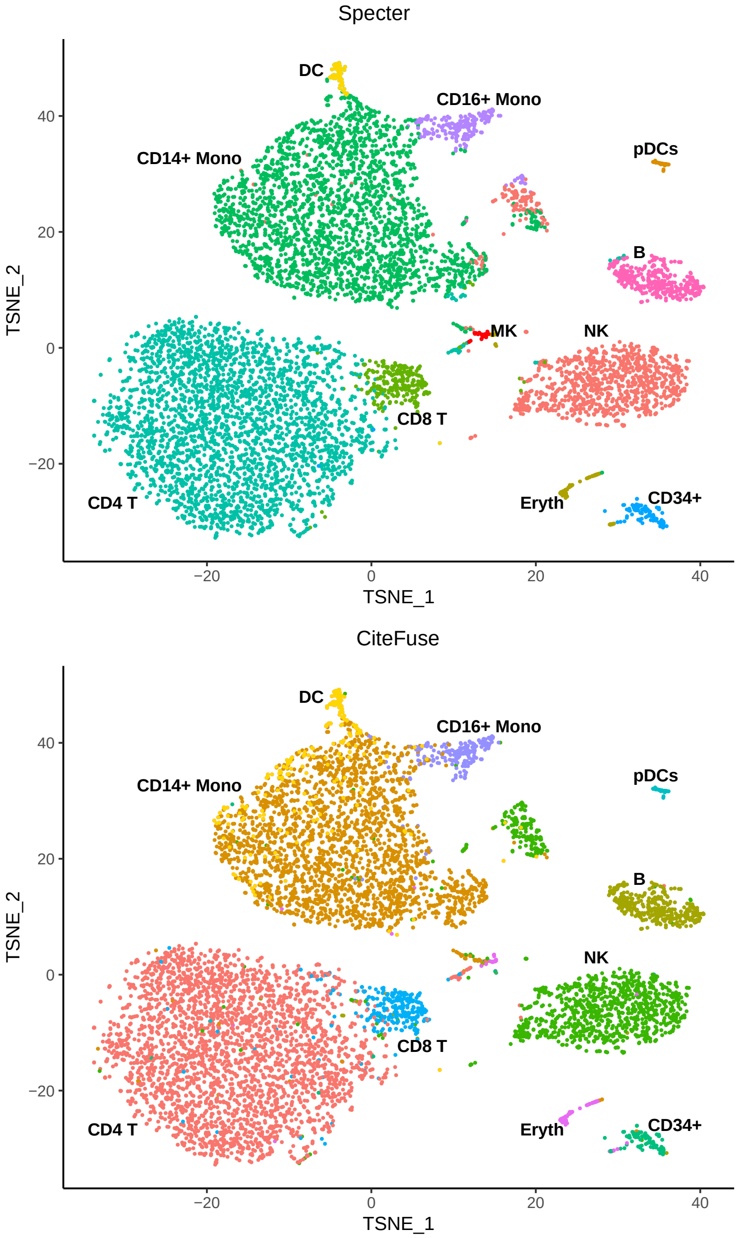

Supplemental Figure S14: Comparison of multimodal clusterings of CBM cells as computed by Specter (top) and CiteFuse (bottom). Despite an overall high agreement between the two clusterings (ARI 0.94), only Specter detects a rare population of megakaryocytes (red).

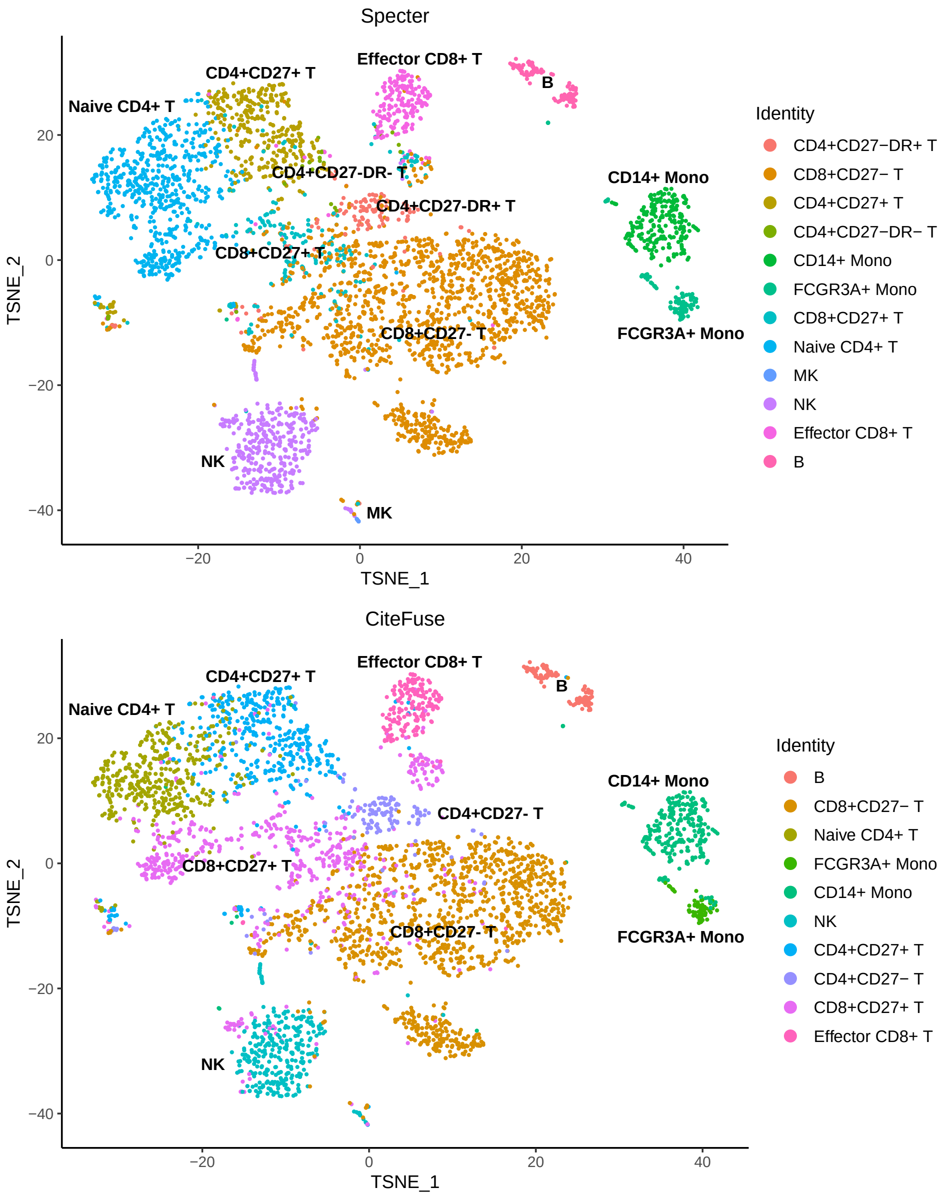

Supplemental Figure S15: Comparison of multimodal clusterings of PBM cells as computed by Specter (top) and CiteFuse (bottom). Despite an overall high agreement between the two clusterings (ARI 0.86), only Specter detects a rare population of megakaryocytes and can discriminate between CD27$^-$DR$^+$ and CD27$^-$DR$^-$ subpopulations of CD4$^+$ memory T cells.

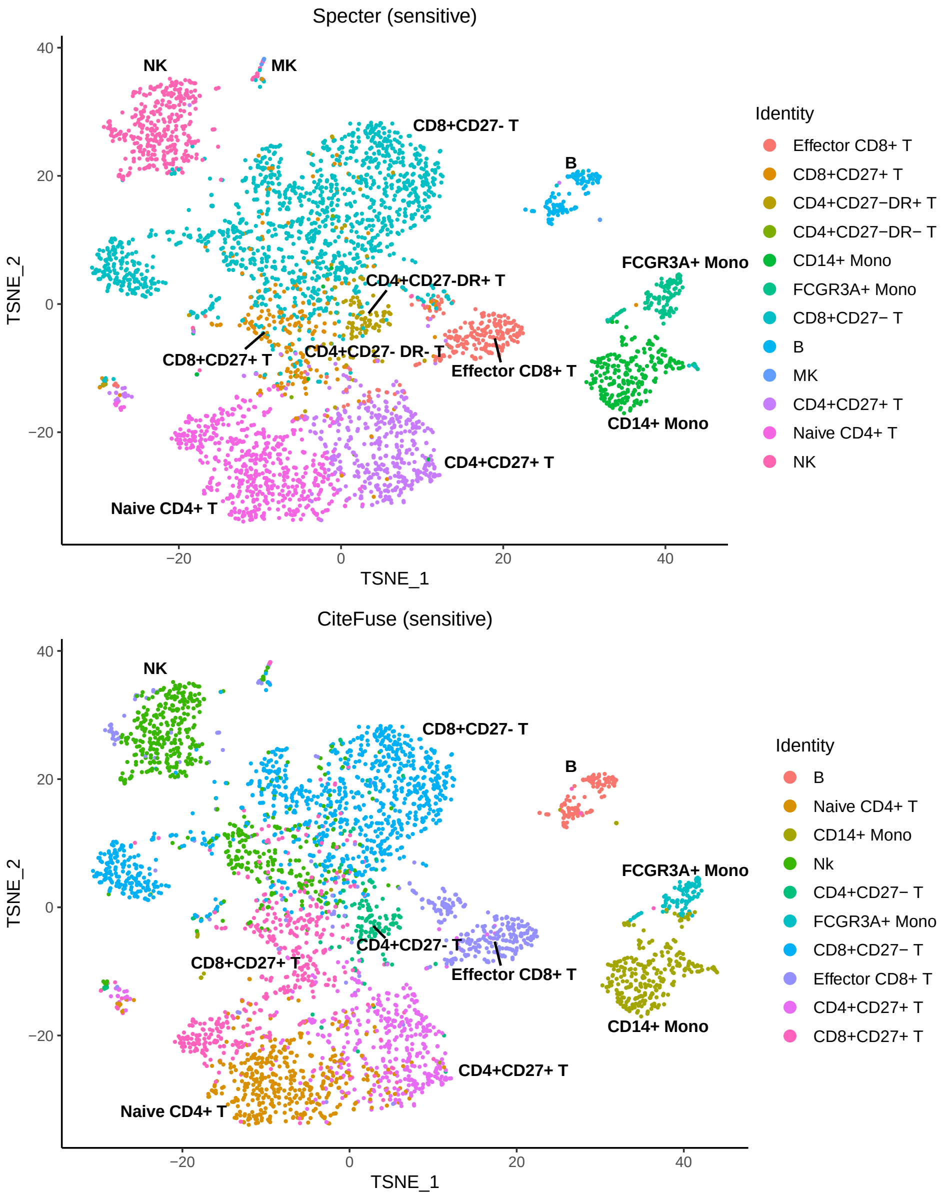

Supplemental Figure S16: Comparison of multimodal clusterings of PBM cells. Here, Specter (top) and CiteFuse (bottom) use slightly more conservative parameters in the doublet removal (eps $= 190$, minPts $= 10$). Again, only Specter is able to discriminate between CD27^{-}DR^{+} and CD27^{-}DR^{-} subpopulations of CD4^{+} memory T cells and detects a rare population of megakaryocytes.

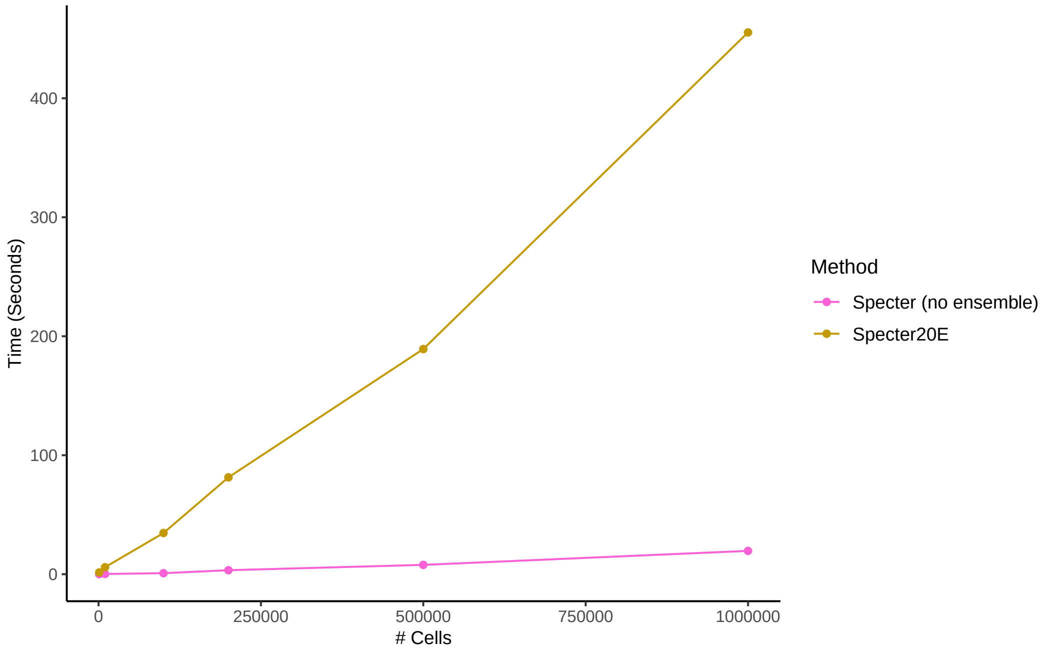

Supplemental Figure S17: Linear-time complexity of Specter. CPU times in seconds (single threaded) are shown for the core algorithm of Specter (no ensemble) and Specter using a clustering ensemble of size 20. Different size data set were simulated using Splatter containing 1k, 10k, 100k, 200k, 500k, and 1 million cells.

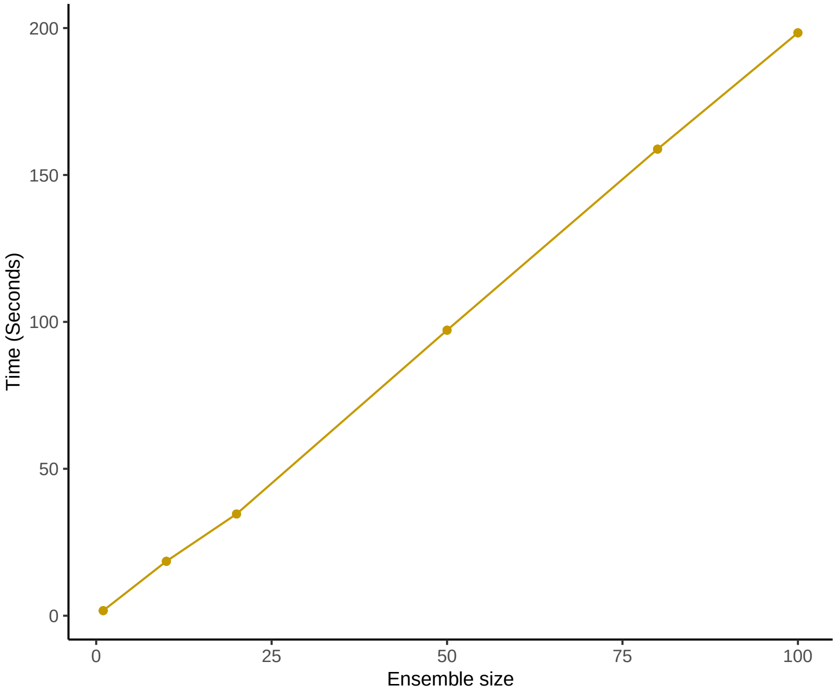

Supplemental Figure S18: Linear increase in running time with number of ensemble members. CPU times in seconds (single threaded) are shown for Specter using an increasing number of ensemble members on a simulated data set containing 100,000 cells.

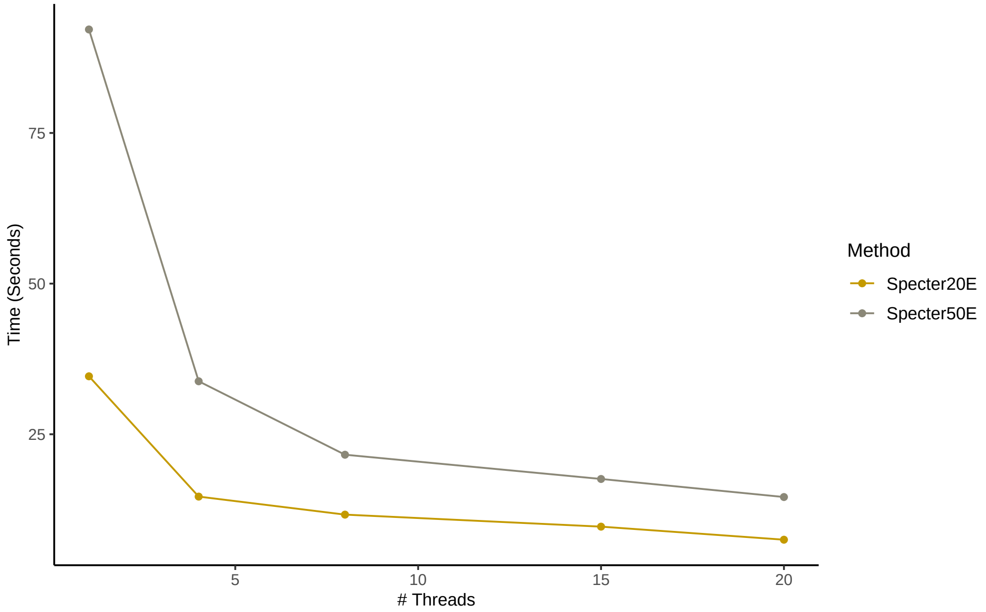

Supplemental Figure S19: Specter speed-up with number of threads. CPU times in seconds are shown for Specter using an increasing number of threads on a simulated data set containing 100,000 cells. 20 or 50 clustering ensemble members were used.

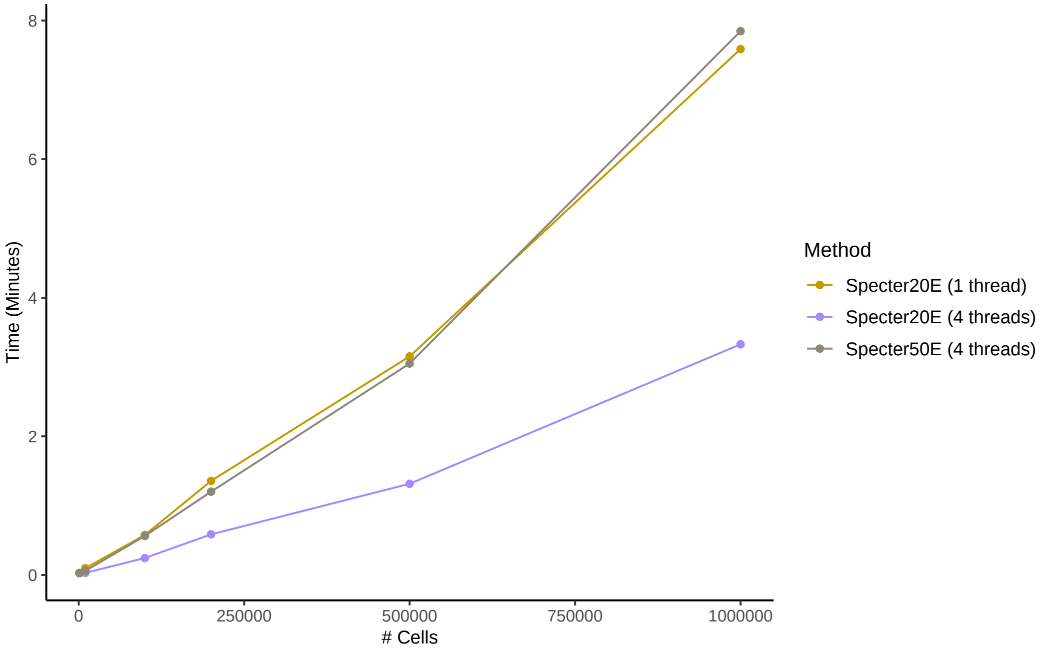

Supplemental Figure S20: Increase in running time for fixed number of threads. CPU times in minutes are shown for Specter using 20 or 50 clustering ensemble members and 1 or 4 threads.

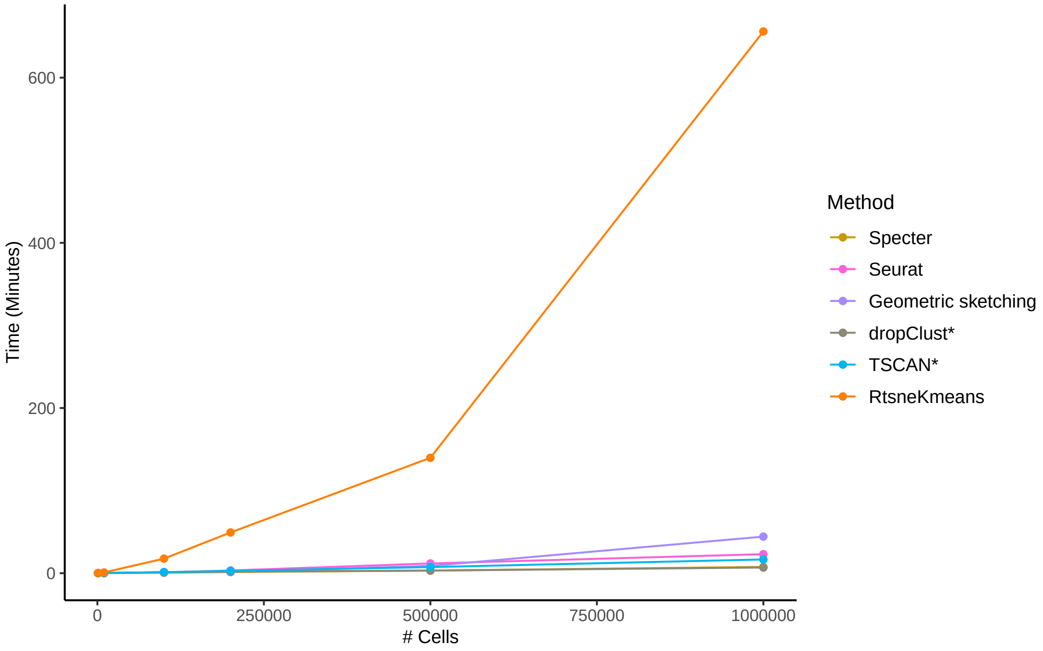

Supplemental Figure S21: Runtime comparison between methods as a function of sample size. CPU times are shown in minutes on different numbers of cells sampled from a simulated data set containing 1 million cells. Seurat was run with a call to the more efficient SCANPY implementation of the Louvain clustering algorithm. *Running times exclude preprocessing for all methods except TSCAN and dropClust, whose implementation did not allow to isolate the core algorithm.

References

Baron M et al. 2016. A Single-Cell Transcriptomic Map of the Human and Mouse Pancreas Reveals Inter- and Intra-cell Population Structure. *Cell Systems.* **3**: 346–360.e4.

Biase FH, Cao X, and Zhong S. 2014. Cell fate inclination within 2-cell and 4-cell mouse embryos revealed by single-cell RNA sequencing. *Genome Research.* **24**: 1787–1796.

Cao J et al. 2019. The single-cell transcriptional landscape of mammalian organogenesis. *Nature.* **34**: 65–31.

Chen R, Wu X, Jiang L, and Zhang Y. 2017. Single-Cell RNA-Seq Reveals Hypothalamic Cell Diversity. *Cell Reports.* **18**: 3227–3241.

Collin M, McGovern N, and Haniffa M. 2013. Human dendritic cell subsets. *Immunology.* **140**: 22–30.

Colpitts SL, Dalton NM, and Scott P. 2009. IL-7 receptor expression provides the potential for long-term survival of both CD62L high central memory T cells and Th1 effector cells during Leishmania major infection. *Journal of Immunology.* **182**: 5702–5711.

Deng Q, Ramsköld D, Reinius B, and Sandberg R. 2014. Single-cell RNA-seq reveals dynamic, random monoallelic gene expression in mammalian cells. *Science.* **343**:

Fonseka CY, Rao DA, Teslovich NC, Korsunsky I, and al. et. 2018. Mixed-effects association of single cells identifies an expanded effector CD4+ T cell subset in rheumatoid arthritis. *Science Translational Medicine.* **10**:

Goolam M, Scialdone A, Graham SJ, Macaulay IC, Jedrusik A, Hupalowska A, Voet T, and Marioni JC. 2016. Heterogeneity in Oct4 and Sox2 Targets Biases Cell Fate in 4-Cell Mouse Embryos. *Cell.* **165**: 61–74.

Grün D et al. 2016. De Novo Prediction of Stem Cell Identity using Single-Cell Transcriptome Data. *Cell Stem Cell.* **19**: 266–277.

Haining WN, Angelosanto J, Brosnahan K, Ross K, Hahn C, Russell K, Drury L, Norton S, Nadler L, and Stegmaier K. 2008. High-throughput gene expression profiling of memory differentiation in primary human T cells. *BMC Immunology.* **9**:

Hruz T, Laule O, Szabo G, Wessendorp F, Bleuler S, Oertle L, Widmayer P, Gruissem W, and Zimmermann P. 2008. Genevestigator V3: A Reference Expression Database for the Meta-Analysis of Transcriptomes. *Advances in Bioinformatics.* **2008**: 1–5.

Klein AM, Mazutis L, Akartuna I, Tallapragada N, Veres A, Li V, Peshkin L, Weitz DA, and Kirschner MW. 2015. Droplet Barcoding for Single-Cell Transcriptomics Applied to Embryonic Stem Cells. *Cell.* **161**: 1187–1201.

Koh PW, Sinha R, Barkal AA, Morganti RM, Chen A, Weissman IL, Ang LT, Kundaje A, and Loh KM. 2016. An atlas of transcriptional, chromatin accessibility, and surface marker changes in human mesoderm development. *Scientific Data.* **3**: 160109.

Kumar RM et al. 2014. Deconstructing transcriptional heterogeneity in pluripotent stem cells. *Nature.* **516**: 56–61.

Lambert MP, Meng R, Harper D, Xiao L, Marks MS, and Poncz M. 2014. Megakaryocytes exchange significant levels of their alpha-granular PF4 with their environment. *Blood.* **124**: 1432–1432.

Lambert MP, Meng R, Xiao L, Harper DC, Marks MS, Kowalska AM, and Poncz1 M. 2016. Intramedullary megakaryocytes internalize released platelet factor 4 (PF4) and store it in alpha granules. *Journal of Thrombosis and Haemostasis.* **13**: 1888–1899.

Linderman GC, Rachh M, Hoskins JG, Steinerberger S, and Kluger Y. 2019. Fast interpolation-based t-SNE for improved visualization of single-cell RNA-seq data. *Nature Methods.* **16**: 243–245.

Merad M, Sathe P, Helft J, Miller J, and Mortha A. 2013. The dendritic cell lineage: ontogeny and function of dendritic cells and their subsets in the steady state and the inflamed setting. *Annual Review of Immunology.* **31**: 563–604.

Muraro MJ et al. 2016. A Single-Cell Transcriptome Atlas of the Human Pancreas. *Cell Systems.* **3**: 385–394.e3.

Ogawa K, Takamori Y, Suzuki K, Nagasawa M, Takano S, Kasahara Y, Nakamura Y, Kondo S, Sugamura K, and Nagata K. 2003. Granulysin in human serum as a marker of cell-mediated immunity. *European Journal of Immunology.* **33**: 1925–1933.

Patel AP et al. 2014. Single-cell RNA-seq highlights intratumoral heterogeneity in primary glioblastoma. *Science.* **344**: 1396–1401.

Pollen AA et al. 2014. Low-coverage single-cell mRNA sequencing reveals cellular heterogeneity and activated signaling pathways in developing cerebral cortex. *Nature Biotechnology.* **32**: 1053–1058.

Sakurai K, Fujiwara T, Hasegawa S, Okitsu Y, Fukuhara N, Onishi Y, Yamada-Fujiwara M, Ichinohasama R, and Harigae H. 2016. Inhibition of human primary megakaryocyte differentiation by anagrelide: a gene expression profiling analysis. *International Journal of Hematology.* **104**: 190–199.

Saunders A et al. 2018. Molecular Diversity and Specializations among the Cells of the Adult Mouse Brain. *Cell.* **174**: 1015–1030.e16.

Turman MA, Yabe T, McSherry C, Bach FH, and Houchins JP. 1993. Characterization of a novel gene (NKG7) on human chromosome 19 that is expressed in natural killer cells and T cells. *Human Immunology.* **36**: 34–40.

Vijayan V. 2020. Fast SVD and PCA. `https://www.mathworks.com/matlabcentral/fileexchange/47132-fast-svd-and-pca`. MATLAB Central File Exchange. Retrieved October 30, 2020.

Xin Y, Kim J, Okamoto H, Ni M, Wei Y, Adler C, Murphy AJ, Yancopoulos GD, Lin C, and Gromada J. 2016. RNA Sequencing of Single Human Islet Cells Reveals Type 2 Diabetes Genes. *Cell Metabolism.* **24**: 608–615.

Zappia L, Phipson B, and Oshlack A. 2017. Splatter: simulation of single-cell RNA sequencing data. *Genome Biology.* **18**: 174.

Zheng GXY et al. 2017. Massively parallel digital transcriptional profiling of single cells. *Nature Communications.* **8**: 14049.